CMS Physics Analysis Summary

Contact: cms-pag-conveners-higgs@cern.ch

Search for a charged Higgs boson decaying into top and bottom quarks in proton-proton collisions at $\sqrt{s} = 13$ TeV in events with electrons or muons

The CMS Collaboration

Abstract

A search is presented for a charged Higgs boson heavier than the top quark and decaying into a top-bottom quark-antiquark pair. Events are selected by the presence of a single isolated charged lepton (electron or muon) or an opposite sign dilepton (electron or muon) pair, categorized according to the jet multiplicity and the number of jets containing a b-hadron decay, and multivariate techniques are used to enhance the signal-background discrimination in each category. This search is based on proton-proton collision data collected by the CMS experiment at the LHC at a center-of-mass energy of 13 TeV, corresponding to an integrated luminosity of 35.9 fb^{-1}. The data are compatible with the standard model, and 95% CL upper limits of 9.6–0.01 pb are set on the product of the charged Higgs boson production cross section and the branching fraction to top-bottom quark-antiquark pair, with mass from 200 GeV to 3 TeV. The upper limits are interpreted in different minimal supersymmetric extensions of the standard model.

1 Introduction

Since the discovery of a Higgs boson [1–3] with a mass of approximately 125 GeV [4, 5], the ATLAS and CMS Collaborations have actively searched for additional neutral and charged Higgs bosons. Most theories beyond the standard model (SM) of particle physics enrich the SM Higgs sector, of which one of the simplest extension predicts the existence of two Higgs doublets [6–8]. Such models are collectively labeled as *two-Higgs-doublet models* (2HDM), and further classified according to the couplings of the doublets to fermions. In Type-I models, only one doublet couples to the fermions, while in Type-II models one doublet couples to the up quarks and the other to the down quarks and the charged leptons. In the lepton-specific model one doublet couples only to the leptonic sector and the other to the quarks, while in the flipped model the first couples specifically to the down quarks and the second one to the up quarks and charged leptons.

The two-doublet structure of the 2HDM Higgs sector gives rise to five physical Higgs bosons through spontaneous symmetry breaking: a charged pair ($H^{\pm}$) and three neutral bosons, namely the light (h) and heavy (H) scalar Higgs bosons, and one pseudoscalar boson (A). Supersymmetric (SUSY) models have a Higgs sector based on 2HDMs. Among the SUSY models, a popular one is the minimal supersymmetric extension to the standard model (MSSM) [9, 10], which has the Higgs sector described by a Type-II 2HDM. In the MSSM, the properties of these particles at tree level are described by two free parameters, which can be chosen as the mass of the charged Higgs boson ($m_{H^{\pm}}$) and the ratio of the vacuum expectation values of the two Higgs doublets ($\tan\beta$).

The detection of a charged Higgs boson would unequivocally point to physics beyond the SM. Model-independent searches for charged Higgs bosons in specific decay modes allow disentangling the Higgs sector physics from the specificity and complexity of the theoretical model and are therefore of utmost interest for the CERN LHC physics program.

The charged Higgs boson production and decay depend on the parameters of the model; charged Higgs bosons with a mass below the top quark mass are dominantly produced in top quark decays, whereas charged Higgs bosons with a mass larger than the top quark mass are produced in association with a top quark, as illustrated in Fig. 1. The charged Higgs boson production at finite order in perturbation theory is accomplished in association with a t and a b quark in the so-called *four-flavor scheme* (4FS) and in association with a t quark in the *five-flavor scheme* (5FS) [11].

In this note, only charged Higgs bosons with a mass larger than the mass of the top quark are considered (*heavy charged Higgs bosons*) and charge-conjugate processes are implied.

The decay of a heavy charged Higgs boson can occur through several channels, amongst them the $H^+ \to \tau^+\nu_\tau$ and $H^+ \to t\bar{b}$ having the highest branching fraction respectively at low and high $m_{H^{\pm}}$ for a large spectrum of $\tan\beta$ and a large variety of theoretical models [12].

Direct searches for the charged Higgs bosons have been performed by LEP and Tevatron experiments and indirect constraints have been set from flavor physics measurements [13–16]. Searches for a charged Higgs boson decaying into top and bottom quarks have been performed by the ATLAS and CMS Collaborations in proton-proton (pp) collisions at a center of mass energy of $\sqrt{s} = 8$ TeV [17, 18] and $\sqrt{s} = 13$ TeV [19]. The ATLAS and CMS Collaborations have also conducted searches for the production of a charged Higgs boson in the $\tau^+\nu_\tau$ [17, 20–22], $c\bar{s}$ [23], and $c\bar{b}$ [24] decay channels at $\sqrt{s} = 8$ and 13 TeV.

Searches for charged Higgs bosons produced via vector boson fusion and decay via W and Z

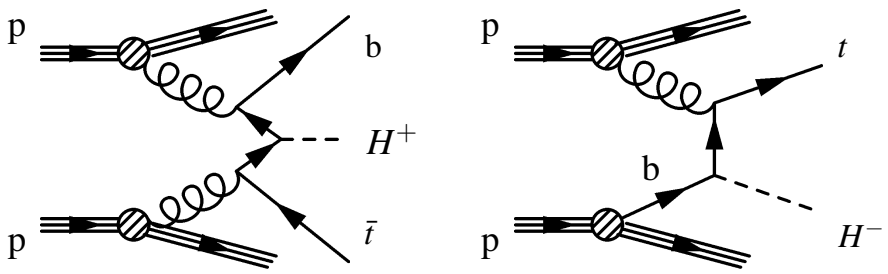

Figure 1: Feynman diagrams for the production of a heavy charged Higgs boson in the four-flavor scheme (4FS, left) and in the five-flavor scheme (5FS, right).

bosons as predicted by the models containing Higgs triplets [25, 26] and searches for additional neutral heavy Higgs bosons decaying to a pair of third generation fermions $\mathrm{t\bar{t}}$, $\mathrm{b\bar{b}}$ and $\tau\overline{\tau}$ [26–30] extend the program of ATLAS and CMS Collaborations to elucidate the extended Higgs sector beyond SM.

This note describes a search for a heavy charged Higgs boson decaying into a top and a bottom quark performed with $35.9\,\mathrm{fb}^{-1}$ of pp collision data collected at a center-of-mass energy of 13 TeV in 2016. The associated production with a top quark involves the presence of two W bosons, in which one or both can decay to leptons (single-lepton and dilepton final states, respectively). The leptonic decays of tau leptons involved in the W boson decay are considered as well. The single-lepton final state is characterized by the presence of one isolated lepton (e, μ) that is used to trigger the event, while the dilepton final state contains cleaner events with two isolated opposite sign leptons ($\mathrm{e^+e^-}$, $\mathrm{e^\pm}\mu^\mp$, $\mu^+\mu^-$). This leads to the suppression of several backgrounds that heavily contaminate the fully hadronic final state. Furthermore, the signal process ($\mathrm{\bar{t}bH^+}$) has a large b jet multiplicity and an additional classification of the events is achieved based on the number of jets identified as originating from decays of b quarks.

Multivariate analysis (MVA) techniques are used to enhance the discrimination between signal and background. The signal-rich regions are analyzed together with the signal-depleted regions in a maximum likelihood fit to the MVA classifier outputs, which simultaneously determines the contributions from the $\mathrm{\bar{t}bH^+}$ signal and the backgrounds.

Model-independent upper limits on the product of the charged Higgs production cross section and the branching fraction into a top-bottom quark-antiquark pair, $\sigma_{\mathrm{H^\pm}}\mathcal{B}(\mathrm{H^\pm \to tb}) = \sigma(\mathrm{pp} \to \mathrm{H^+\bar{t}b})\mathcal{B}(\mathrm{H^+ \to t\bar{b}}) + \sigma(\mathrm{pp} \to \mathrm{H^-t\bar{b}})\mathcal{B}(\mathrm{H^- \to \bar{t}b})$, as a function of the $m_{\mathrm{H^\pm}}$ are presented in this note. Results are also interpreted in specific MSSM benchmark scenarios, where the underlying free parameters are fixed by the specific scenario.

2 The CMS detector

The central feature of the CMS apparatus is a superconducting solenoid of 6 m internal diameter, providing a magnetic field of 3.8 T. Within the solenoid volume are a silicon pixel and strip tracker, a lead tungstate crystal electromagnetic calorimeter (ECAL), and a brass and scintillator hadron calorimeter (HCAL), each composed of a barrel and two endcap sections. Forward calorimeters extend the pseudorapidity coverage provided by the barrel and endcap detectors. Muons are detected in gas-ionization chambers embedded in the steel flux-return yoke outside

the solenoid. Events of interest are selected using a two-tiered trigger system [31]. The first level, composed of specialized hardware processors, uses information from the calorimeters and muon detectors, while the second level consists of a farm of processors running a version of the full event reconstruction software optimized for fast processing. A more detailed description of the CMS detector, together with a definition of the coordinate system used and the relevant kinematic variables, can be found in Ref. [32].

3 Event simulation

Signal events are simulated using the MADGRAPH5_aMC@NLO v2.3.3 [33] generator at the next-to-leading order (NLO) precision in perturbative quantum chromodynamics using the 4FS for a range of $m_{\mathrm{H}^{\pm}}$ hypotheses between 200 GeV and 3 TeV.

The main SM background to this analysis originates from top quark pair production. Other backgrounds considered are the production of W and Z/γ^* with additional jets (referred to as V+jets), diboson and triboson processes, single top quark production, $\mathrm{t\bar{t}}$ production in association with W, Z, γ, H, $\mathrm{t\bar{t}}$, and QCD multijet events.

The $\mathrm{t\bar{t}}$ and single top quark events in the *t*- and t W-channels are generated with POWHEG v2.0 [34]. The MADGRAPH5_aMC@NLO 2.2.2 generator [33] at LO, with MLM matching [35], is used to generate vector boson in association with jets and single top quark events in the *s*-channel. The associated production of $\mathrm{t\bar{t}}$ events with a vector boson is simulated at NLO using MADGRAPH5_aMC@NLO v2.2.2 with FxFx jet matching and merging [36].

In all cases, the NNPDF3.0 [37] set of parton distribution function (PDF) is used and the parton showers and hadronization processes are performed by PYTHIA 8.2 [38] with the CUETP8M1 [39] tune for the underlying event, except for the $\mathrm{t\bar{t}}$ sample where the tune CUETP8M2T4 [40] provides a more accurate description of the kinematic distributions of the top quarks and of the jet multiplicity.

The production cross section for the heavy charged Higgs boson signals have been computed in the 4FS and 5FS schemes, and combined together to obtain the total cross section using the *Santander matching* scheme [11] for different values of $\tan\beta$. Typical values are of the order of 1 pb for a mass of 200 GeV, down to about 10^{-4} pb for a mass of 3 TeV [12, 41–45]. Branching fractions $\mathcal{B}(\mathrm{H}^+ \to \mathrm{t\bar{b}})$have been computed in the chosen scenarios with the HDECAY package [46].

Next-to-NLO (NNLO) calculations are used to compute the cross section for the dominant $\mathrm{t\bar{t}}$ background for a top quark mass of 172.5 GeV, including resummation to next-to-next-to-leading-logarithmic accuracy [47–53]. The other backgrounds are normalized using NLO (single top quark *t*- and *s*-channels [54, 55], $\mathrm{t\bar{t}}$+V production [56], and diboson production [57]), NNLO (V+jets production), and approximate NNLO (single top quark tW-channel [58]) cross sections.

The simulated $\mathrm{t\bar{t}}$ sample is further separated into the following processes, based on the flavor of additional jets that do not originate from the top quark decays in the event and are labeled according to their content in b- and c-originated hadrons. The $\mathrm{t\bar{t}}$+b($\mathrm{\bar{b}}$) ($\mathrm{t\bar{t}}$+c($\mathrm{\bar{c}}$)) label is attributed to the events that have at least one b jet (c jet and no b jet) from the event generator within the acceptance. The events that do not belong to any of the above processes are enriched in light flavor jets and therefore denominated $\mathrm{t\bar{t}}$+LF. This partition of the $\mathrm{t\bar{t}}$ simulated sample is introduced to account for different systematic uncertainties affecting the corresponding cross section predictions.

All generated events are passed through a detailed simulation of the CMS apparatus, based on GEANT4 v9.4 [59]. The effects for additional pp interactions occurring in the same or in neighboring bunch crossings (pileup) are modeled by adding simulated minimum bias events to all simulated processes. In the data collected in 2016, an average of 23 pp interactions occurred per LHC bunch crossing. In simulation, the difference in the number of true interactions is accounted for by reweighting the simulated events to match the data.

4 Object reconstruction

The particle-flow (PF) algorithm [60] aims to reconstruct and identify each individual particle in an event, with an optimized combination of information from the various elements of the CMS detector. The energy of photons is obtained from the ECAL measurement. The energy of electrons is determined from a combination of the electron momentum at the primary interaction vertex as determined by the tracker, the energy of the corresponding ECAL cluster, and the energy sum of all bremsstrahlung photons spatially compatible with originating from the electron track. The momentum of muons is obtained from the curvature of the corresponding track. The energy of charged hadrons is determined from a combination of their momentum measured in the tracker and the matching ECAL and HCAL energy deposits, corrected for zero-suppression effects and for the response function of the calorimeters to hadronic showers. Finally, the energy of neutral hadrons is obtained from the corresponding corrected ECAL and HCAL energy. The reconstructed vertex with the largest value of summed physics-object squared transverse momentum (p_{T}^2) is taken to be the primary pp interaction vertex [61]. The physics objects are the jets, clustered using the jet finding algorithm [62, 63] with the tracks assigned to the vertex as inputs, and the associated missing transverse momentum, taken as the negative vector sum of the p_{T} of those jets.

Electrons are identified using an MVA identification algorithm [64]. Working points are defined by setting thresholds for the classifier values such that there is no efficiency loss for high-p_{T} electrons, particularly from high-mass signal events; such working points are described as `Tight` (≈88% efficiency for $\mathrm{t\bar{t}}$ events) and `Loose` (≈95% efficiency for $\mathrm{t\bar{t}}$ events). Muon identification uses the algorithm described in Ref. [65]; two working points are used in the analysis referred to as `Loose` and `Tight` with efficiencies close to 99% and 99.9%, respectively. Efficiencies in triggering, reconstruction, identification, and isolation of leptons are estimated both in data and simulation. Those efficiencies are used to determine correction factors between data and simulation depending on p_{T} and η, and are applied to each lepton used in this analysis.

Electrons and muons are required to be isolated from other particles by measuring their relative isolation as the ratio between the scalar p_{T} sum of selected PF particles within a cone of a radius decreasing with lepton p_{T}.

Jets are reconstructed from the PF particles clustered by the anti-k_{T} algorithm [62, 63] with a clustering radius of 0.4. To mitigate the effect of pileup interactions, charged hadrons that do not arise from the primary vertex are removed from the clustering algorithm. Furthermore, jets fully originating from pileup interactions are removed by means of an MVA identification algorithm [66]. The jet momentum is then corrected in simulated events to account for multiple effects, including the extra energy clustered in jets arising from pileup. Jets are selected if they satisfy $p_{\mathrm{T}} > 40\,\mathrm{GeV}$ and $|\eta| < 2.4$. Loose identification criteria are applied to the jets, in order to distinguish them from well identified stable particles. Finally, jets are required to be well separated from the selected leptons by $\Delta R > 0.4$, where ΔR is defined as $\sqrt{(\Delta\eta)^2 + (\Delta\phi)^2}$ and $\Delta\eta$ and $\Delta\phi$ are the distances in the pseudorapidity and azimuthal angle.

Jets from the hadronization of the b quark are identified (b-tagged) using the *combined secondary vertex* algorithm [67]. The mistagging probability—the fraction of jets that arise from the fragmentation of light partons (u, d, s, and g) and c jets misidentified by the algorithm as a b jet—is approximately 1% and 15%, respectively, while the efficiency to correctly identify a b jet is about 70%. The difference in b tagging and mistagging efficiencies between data and simulation is corrected by applying data-to-simulation correction factors dependent on the jet p_T and η.

The missing transverse momentum vector ($\vec{p}_T^{\,miss}$) is defined as the projection of the negative vector sum of the momenta of all reconstructed PF particles in an event onto the plane perpendicular to the beams. Its magnitude is referred to as p_T^{miss}. The p_T^{miss} reconstruction is improved by propagating the jet energy corrections to it. Further filtering algorithms are used to reject events with anomalously large p_T^{miss} resulting from instrumental effects [68].

Hadronically decaying τ leptons (τ_h) are reconstructed using the *hadron-plus-strips* algorithm [69], based on the identification of the individual τ decay modes. The τ_h candidates compatible with electrons or muons are rejected. Jets originating from the hadronization of quarks and gluons are suppressed by requiring that the τ_h candidate is isolated. The τ_h identification efficiency depends on $p_T^{\tau_h}$ and η^{τ_h}, and is on average 50% for $p_T^{\tau_h} > 20\,\text{GeV}$ with a probability of approximately 1% for hadronic jets to be misidentified as a τ_h. The isolation variable is constructed from the PF particles inside a cone of $\Delta R = 0.3$. The effect of neutral PF candidates from pileup vertices is estimated using charged hadrons associated with those vertices and subtracted from the isolation variable.

5 Event selection and classification

Events are selected with single-lepton triggers characterized by transverse momentum thresholds of 24 (27) GeV for muons (electrons). Additionally, several paths with higher p_T thresholds and looser identification requirements are included to maximize efficiency for high-p_T muons and electrons, resulting in an overall efficiency in the plateau region close to 95% and 100%, respectively. Correction factors quantifying the difference between trigger efficiencies in data and simulated events are evaluated using a tag-and-probe procedure [64, 65].

Events are required to have at least one muon (electron) with $p_T > 30\,\text{GeV}$ ($> 35\,\text{GeV}$) satisfying tighter identification and isolation criteria than the online requirements. As briefly discussed in Section 1, the first classification is achieved by separating the events in five single-lepton and dilepton categories ($e^{\pm}$, $\mu^{\pm}$, e^+e^-, $e^{\pm}\mu^{\mp}$, $\mu^+\mu^-$). In the single-lepton category, only events with exactly one lepton are accepted, whereas the presence of any additional lepton passing the loose identification requirements with $p_T > 10\,\text{GeV}$ vetoes the event. Moreover, the presence of a τ_h with $p_T > 20\,\text{GeV}$ and $|\eta| < 2.3$ vetoes the event. In the dilepton category, we accept events with exactly two oppositely charged leptons (electrons or muons), with the looser identification criteria on the second lepton. To reduce the Drell–Yan background, we reject events with two leptons of the same flavor and opposite charge with the invariant mass $m_{\ell\ell}$ less than 12 GeV or between 76 and 106 GeV.

The final states examined in this note include neutrinos coming from the W boson decays. Therefore events are required to have $p_T^{miss} > 30\,\text{GeV}$. Additionally, in the single-lepton final state events in which the p_T^{miss} is compatible with mismeasurement of electron or jet energy removed by requiring the $\Delta\Phi$ between p_T^{miss} and any jet in the event to be larger than 0.05.

Signal events are characterized by having at least five (three) jets at LO in the final state corre-

sponding to semileptonic (dileptonic) decays of the W bosons. The $\mathrm{t\bar{t}}$ background has a lower jet multiplicity in the corresponding categories, but additional jets may be produced through initial- and final-state radiation. Requiring a high multiplicity of reconstructed jets improves the discrimination of signal events from the SM background while the regions enhanced in SM background processes constrain background estimates using data. Consequently, the single-lepton and dilepton event categories require the presence of at least four and two jets, respectively. The SM top quark pair production has similar final states with fewer b quarks in the leading order (LO) production, while additional gluon splitting contaminates the high b jet multiplicity regions. Consequently, one or more of these jets must be b-tagged.

Events are further categorized according to the total number of associated jets and the b-tagged jet multiplicity, yielding a total of nine categories in the single-lepton final state and eight categories in the dilepton final state. In the single-lepton final state, the subcategories are: ($4j/1$b), ($4j/2$b), ($4j/\geq 3$b), ($5j/1$b), ($5j/2$b), ($5j/\geq 3$b), ($\geq 6j/1$b), ($\geq 6/2$b), and ($\geq 6j/\geq 3$b); while in the dilepton final states, where less hadronic activity is expected, the subcategories are: ($2j/1$b), ($2j/2$b), ($3j/1$b), ($3j/2$b), ($3j/3$b), ($\geq 4j/1$b), ($\geq 4j/2$b), and ($\geq 4j/\geq 3$b). The resulting regions are characterized by different background compositions and signal purities. The highest significance for both the single- and the dilepton final states is found in the high jet and b jet multiplicity categories, for a large H^+ mass range, except for the low jet and b jet multiplicity categories for H^+ mass signals around $\approx 200\,\mathrm{GeV}$. Finally, events with two same-sign leptons are used to form control regions for the multijet background estimation.

A set of discriminant variables are selected to enhance the signal and background separation in each subcategory. Kinematic and topological shapes have a different discrimination power for the different mass hypotheses of the charged Higgs boson. Each discriminant variable is studied and included in the MVA classifier if it improves the discrimination, or otherwise discarded. Commonly to the single- and dilepton categories, the H_T distribution, defined as the scalar sum of the transverse momenta of the selected jets, is one of the most sensitive variables. Additionally, the largest transverse momentum among the b jets, the $p_\mathrm{T}^\mathrm{miss}$, the minimum invariant mass between the lepton and the b jets, the rapidity gap between the two farthest b-tagged jets in the η–ϕ plane, the smallest ΔR separation of the b jets, and the p_T weighted average of the b tagging discriminator among the non-b-tagged jets are used as input variables in the MVA discriminators. Information on the event topology is incorporated via event shape variables such as such as the centrality defined as the ratio of the sum of the transverse momentum of all jets and their total energy, and the second Fox–Wolfram moment [70] calculated using all jets.

In the single-lepton final states, the following variables are also included: the invariant mass of the three jets with largest transverse momentum, the transverse mass of the system constituted by the lepton and the missing transverse momentum, the angular separation between the lepton and the system constituted by the b jet pair with the least ΔR separation between the b jets, and the average separation between the b jet pairs.

The even selection for the dilepton final state takes advantage of the presence of the second lepton. The lepton with largest transverse momentum (leading lepton) characterizes the decay of a boosted top quark that comes from the massive charged Higgs boson in the signal hypothesis. The following variables are also considered: the ΔR between the leading lepton and the leading b-tagged jet, the momentum of the leading lepton, the lepton p_T asymmetry, the mass of the lepton and b-tagged jet with the largest transverse momentum, and the smallest of the transverse masses constructed with the leading b jet and each of the two W boson hypotheses, where the W bosons are reconstructed using the $\vec{p}_\mathrm{T}^\mathrm{miss}$ and the lepton momenta.

A summary of the discriminating variables is reported in Table 1.

Table 1: Summary of the discriminating variables used in the analysis of the single-lepton (1ℓ) and dilepton (2ℓ) final states.

1ℓ and 2ℓ	H_{T}	Scalar sum of the jet transverse momenta
	p_{Tb}	Largest transverse momentum among the b-tagged jets
	$p_{\mathrm{T}}^{\mathrm{miss}}$	Missing transverse momentum
	$\min m(\ell,\mathrm{b})$	Minimum invariant mass between the lepton and the b-tagged jet
	$\max \Delta\eta(\mathrm{b},\mathrm{b})$	Maximum pseudorapidity separation between b-tagged jet pairs
	$\min \Delta R(\mathrm{b},\mathrm{b})$	Minimum separation between b-tagged jet pairs
	p_{T}-ave CSV	p_{T} weighted average of the combined secondary vertex discriminator of the non-b-tagged jets
	FW_2	Second Fox–Wolfram moment
	centrality	Ratio of the sum of the transverse momentum and the total energy of all jets
1ℓ	m_{jjj}	Invariant mass of the jet system composed by the first three jets ranked in p_{T}
	$m_{\mathrm{T}}(\ell, \vec{p}_{\mathrm{T}}^{\mathrm{miss}})$	Transverse mass of the system constituted by the lepton and the $\vec{p}_{\mathrm{T}}^{\mathrm{miss}}$
	$\Delta R(\ell,\mathrm{bb})$	Distance between b-tagged jet pair with the smallest ΔR separation and the lepton
	ave$\Delta R(\mathrm{b},\mathrm{b})$	Average separation between b-tagged jet pairs
2ℓ	N_{jets}	Number of selected jets
	$N_{\mathrm{b\,jets}}$	Number of selected b-tagged jets
	$\Delta R(\ell,\mathrm{b})$	Distance between the lepton and the b-tagged jet with largest transverse momenta
	$p_{\mathrm{T}\ell}$	Largest transverse momentum between the leptons
	$\frac{p_{\mathrm{T}\ell 1}-p_{\mathrm{T}\ell 2}}{p_{\mathrm{T}\ell 1}+p_{\mathrm{T}\ell 2}}$	Lepton p_{T} asymmetry
	$m(\ell,\mathrm{b})$	Invariant mass of the lepton and b-tagged jet with the largest transverse momentum (top quark candidate)
	$m_{\mathrm{T}}^{\mathrm{min}}$	$\min\left[m_{\mathrm{T}}(\mathrm{b}, p_{\mathrm{T}\ell 1}+\vec{p}_{\mathrm{T}}^{\mathrm{miss}}), m_{\mathrm{T}}(\mathrm{b}, p_{\mathrm{T}\ell 2}+\vec{p}_{\mathrm{T}}^{\mathrm{miss}})\right]$. The smallest of the transverse masses constructed with the leading b-tagged jet and each of the two W boson hypotheses

Separate classifiers are constructed for the single-lepton and dilepton final states, using different technologies in order to fully exploit the different set of features described above. For each of the suitable discriminating variables, it has been carefully verified that the simulation models the data correctly.

A boosted decision tree (BDT) [71] classifier is trained using the TMVA package [72] to discriminate signal and background in the single-lepton categories. The different kinematic signature of the signal with respect to the $m_{\mathrm{H}^{\pm}}$ is accounted for by having a separate training for each $m_{\mathrm{H}^{\pm}}$ hypothesis. The training process is optimized by targeting a region enriched in signal events by requiring that the number of selected jets $N_{\text{jets}} \geq 5$ and the number of selected b jets $N_{\text{b jets}} \geq 2$ (training region). The binned discriminant of the BDT is calculated in all the single-lepton subcategories corresponding to the training region plus the ($4j/\geq$3b) region and used in the maximum likelihood fit. In the other single-lepton subcategories, the inclusive event yields are used in the fit to infer additional information on the background normalization.

The dilepton final states exploit a novel technology based on deep neural network (DNN) classifiers [71], parametrized as a function of the $m_{\mathrm{H}^{\pm}}$ [73]. The TensorFlow (v1.4.0) backend [74] and the Keras (v2.1.1) frontend [75] are used to train the classifier. The parametrization of the signal events as a function of the $m_{\mathrm{H}^{\pm}}$ enables to have a unique training for all the different signal mass hypotheses. The training process is optimized in the region enriched in signal events by requiring $N_{\text{jets}} \geq 3$ and $N_{\text{b jets}} \geq 1$ or $N_{\text{jets}} \geq 2$ and $N_{\text{b jets}} \geq 3$. The jet and b-tagged jet multiplicities are used in the training parametrization to capture the characteristics of the signal and background processes in the different categories. The binned DNN output is used in the maximum likelihood fit in all the dilepton subcategories to further gauge differences between the different background processes.

Both in the single- and in the dilepton categories, the training process is carefully scrutinized and possible sources of over- or undertraining are verified by means of statistical tests. Disjoint sets of simulated events are used in the training processes and the subsequent steps of the analysis to avoid biases in the results.

The bin size for the MVA output in each of the subcategories of the analysis is chosen with a variable binning strategy such that the statistical uncertainty in signal and background event yields is less than 20% in each bin. In order to avoid possible biases in the binning strategy induced by the statistical fluctuations in the simulated samples, the bin boundaries are defined based on the events used for the MVA training.

6 Background estimation and systematic uncertainties

The semi- and dileptonic decays of the two W bosons in the $\mathrm{t\bar{t}}$ process represent the main background of the analysis for the single-lepton and dilepton final states respectively. The $\mathrm{t\bar{t}}$ production—as discussed in Section 3—is separated into $\mathrm{t\bar{t}}$+LF, $\mathrm{t\bar{t}}$+c($\mathrm{\bar{c}}$), and $\mathrm{t\bar{t}}$+b($\mathrm{\bar{b}}$) processes. The two latter processes are commonly referred to as $\mathrm{t\bar{t}}$+heavy flavor (HF). The categorization strategy described in Section 5 populates the low b jet multiplicity regions with the $\mathrm{t\bar{t}}$+LF process, while the regions enriched with the signal are characterized by a larger contribution of the $\mathrm{t\bar{t}}$+HF processes. Smaller background contributions arise from the single top quark production, the vector boson production in association with jets, the multiboson production processes, $\mathrm{t\bar{t}}$ production in association with electroweak bosons (W, Z, γ, H), and $\mathrm{t\bar{t}t\bar{t}}$ production.

Different sources of experimental and theoretical uncertainties are modeled as nuisance parameters and they are allowed to change the event yield, the migration of events among categories,

and the distribution of the MVA output in each category [76]. Uncertainties that purely affect the yield within a category (rate uncertainties) are modeled through a nuisance with log-normal probability density function, while changes in shapes (shape uncertainties) are performed with a polynomial interpolation with a Gaussian constraint and can also change the event yields. All the sources of systematic uncertainty applied to the analysis are discussed below.

The uncertainty in the luminosity measurement of the 2016 dataset amounts to 2.5% [77]. The uncertainty in the evaluation of the pileup in the simulation is accounted for by varying the minimum bias cross section by $\pm 5\%$ and propagating the variation effect through the reweighting procedure [78]. The difference between the nominal and the altered distributions is taken as the uncertainty and is treated as shape variation in the fit. Both the luminosity and the pileup uncertainties are separately treated as fully correlated among all processes.

Each reconstructed jet is corrected through calibration factors in order to account for the response of the detectors with dependencies on the geometry, the pileup conditions and the kinematic properties of the jet [66]. The uncertainties in the jet energy scale and in the jet energy resolution are propagated by varying the jet momenta and consequently the missing transverse momentum. The events are fully reanalyzed in order to extract the appropriate rate and shape variations for the final distributions. Furthermore, an extra uncertainty accounts for the effect of the unclustered energy scale on the $p_{\mathrm{T}}^{\mathrm{miss}}$. Each of these uncertainties is treated as fully correlated among all processes.

The b tagging and mistagging uncertainties are obtained by varying the corresponding per-jet correction factors upwards and downwards [79]. The mistag efficiency uncertainties for jets originating from light partons (u, d, s, and g) are considered to be uncorrelated with the b tagging efficiency uncertainties, while c-mistag efficiency uncertainties are varied simultaneously with the bottom quark efficiencies. The b tagging and mistagging efficiency uncertainties are doubled whenever they are extrapolated outside the p_{T}/η range of the correction factor derivations. Different sources of uncertainties are varied as independent nuisance parameters. One of the components of the b tagging efficiency uncertainty is correlated with the jet energy scale, reflecting the correlation in the derivation of the correction factors.

The uncertainties in the lepton selection efficiency correction factors—due to trigger, identification, and isolation—are applied as upward and downward variations as a function of the lepton p_{T} and η. The propagation of the correction factors on the shape of the MVA output only impacts the overall normalization. The squared sum of the variations due to the identification, isolation, and trigger efficiencies is therefore included as a single rate uncertainty amounting to 3% (4%) for electrons (muons), treated as correlated among all the final categories.

Small discrepancies between data and simulation are observed in control regions enriched in processes involving a vector boson with additional jets. The Drell–Yan and W +jets H_{T} distributions are matched to the data using corrections derived in a region close to the mass of the Z boson and in the zero b jet control region, respectively. The uncertainties in the derivation of correction factors for the DY and W +jets processes in the H_{T} distribution are accounted for in the final results. They are assumed uncorrelated between the two processes and correlated among the final categories.

The QCD multijet production is a minor background to the analysis and ignored in the limit setting after the verification of the simulation prediction. For the single-lepton categories, the simulation prediction has been checked in an orthogonal set of events requiring that the $p_{\mathrm{T}}^{\mathrm{miss}}$ is aligned with the jets, while for the dilepton categories, the QCD multijet production is verified in the same-sign dilepton control regions for each category defined by the N_{jets} and $N_{\mathrm{b\,jets}}$.

Theoretical uncertainties related to parton density function are applied as rate uncertainties to the simulated background samples and account for both the acceptance and the cross section mismodeling. Uncertainties from factorization and renormalization scales in the inclusive cross sections are considered depending on the process and are estimated by varying the matrix element scales independently from each other by factors of 0.5 and 2 with respect to the default values [80].

For the simulated samples involving a top quark, an additional uncertainty in the cross sections due to the choice of the top quark mass is considered by varying the top quark mass by 1.0 GeV around the nominal value of 172.5 GeV.

The matching of the POWHEG NLO $\mathrm{t\bar{t}}$ matrix element calculation with the PYTHIA parton shower (PS) is varied by shifting the parameter $h_{\mathrm{damp}} = 1.58\,^{0.66}_{-0.59}$ [81] within the uncertainties. These theoretical uncertainties are considered to be uncorrelated among all processes and conservatively also uncorrelated between the single-lepton and dilepton final states. An additional source of uncertainty arises from the modeling of additional jets by the event generator in top quark pair production. This uncertainty is estimated in each bin of jet and b jet multiplicity, based on the simulated $\mathrm{t\bar{t}}$ samples which are enriched/reduced in initial- and final-state radiation. The initial state radiation PS scale is multiplied by factors of 2 and 0.5 in dedicated simulated samples, whereas the final state radiation PS scale is scaled up by $\sqrt{2}$ and down by $1/\sqrt{2}$ [39, 81]. For each perturbation, the uncertainty is evaluated as the relative deviation with respect to the nominal event rates. A nuisance parameter is added for each category defined by N_{jets} and $N_{\mathrm{b\,jets}}$ and decorrelated between the single- and dilepton final states.

The normalization of the $\mathrm{t\bar{t}}$+HF processes is weakly constrained by the theoretical calculations [82] or the experimental measurements. Thus a conservative rate uncertainty of 50% is assigned to each of them, in addition to the cross section uncertainties listed in Table 2. This procedure allows the signal-depleted regions to determine the overall normalization factor, which includes the production cross section, detector acceptance, and reconstruction efficiencies.

The limited size of the background and signal simulated samples results in statistical fluctuations of the nominal prediction. The content of each bin of each final discriminant distribution is varied by its statistical uncertainty. The *Barlow–Beeston lite* approach [83, 84] is applied by assigning, for each bin, the combined statistical uncertainty of all simulated samples to the process dominating the background yield in that bin. Since all bins are statistically independent, each variation is treated as uncorrelated with any other variation.

A summary of the effects of the systematic uncertainties on the final event yields, summed over all final states and categories, is provided in Table 2.

7 Results

The statistical interpretation is based on a simultaneous fit on the MVA output shapes and event yields in the different categories described in Section 5. The parameter of interest reflecting the signal normalization $\sigma_{\mathrm{H}^{\pm}}\mathcal{B}(\mathrm{H}^{\pm} \to \mathrm{tb})$ and the nuisance parameters specified in Section 6 are encoded in a negative log-likelihood function and profiled in the minimization process. The log-likelihood ratio is used as test statistic to assess the agreement with the background-only hypothesis or the presence of the signal and the asymptotic approximation is used in the statistical analysis [76, 85]. The statistical method used to report the results is the $\mathrm{CL_s}$ modified frequentist criterion [86, 87].

Figure 2 shows the event yields in the subcategories of the analysis after a background-only fit

Table 2: Effects of the systematic uncertainties as the percentual variation of the final event yields prior to the fit to the data, summed over all final states and categories.

Source of uncertainty	Shape	$H^{\pm}$	$t\bar{t}$+LF	$t\bar{t}$+c($\bar{c}$)	$t\bar{t}$+b($\bar{b}$)	t,t W,$t\bar{t}$ +X	V+jets
Luminosity		2.5	2.5	2.5	2.5	2.5	2.5
Pileup	✓	0.4	0.2	0.2	0.2	0.2	1.8
Jet energy scale and resolution	✓	2.8	3.9	3.3	3.0	3.9	5.3
b jet identification	✓	4.6	3.1	4.1	4.6	3.0	11.6
Lepton selection efficiency		3.4	3.1	3.3	3.3	3.3	3.7
Unclustered $p_{\mathrm{T}}^{\mathrm{miss}}$ energy scale		2.0	2.0	2.0	2.0	2.0	2.0
Acceptance (QCD scale, PDF)	✓	9.8	9.0	11.4	12.0	3.3	11.2
Cross section (QCD scale, PDF)		—	5.5	5.5	5.5	4.0	4.1
Top quark mass		—	2.7	2.7	2.7	2.2	—
$t\bar{t}$ parton showering		—	6.4	10.6	9.5	—	—
$t\bar{t}$ HF normalization		—	—	50.0	50.0	—	—

to the data. In the regions where the shape of MVA output is used, the yields are obtained by integrating the distribution and the correlations across the bins are accounted for in the quoted uncertainties. The contribution of a hypothetical charged Higgs boson with a mass of 500 GeV and $\sigma_{\mathrm{H}^{\pm}}\mathcal{B}(\mathrm{H}^{\pm}\to\mathrm{tb}) = 10$ pb is also displayed. In the same configuration, Fig. 3 shows the MVA (BDT and DNN) outputs in exemplary signal-region subcategories for the single- ($5j/\geq 3$b) and dilepton final states ($3j/3$b).

The data agree with the SM background distributions and no significant excess is observed. Exclusion limits are set at 95% confidence level (CL) on $\sigma_{\mathrm{H}^{\pm}}\mathcal{B}(\mathrm{H}^{\pm}\to\mathrm{tb})$ for $m_{\mathrm{H}^{\pm}}$ hypotheses between 200 GeV and 3 TeV. The observed (expected) upper limits with single- and dilepton final states combined are shown in Fig. 4 and listed in Table 3. The single-lepton and dilepton categories have comparable sensitivity in the low mass regime (≈200 GeV) while the single-lepton categories become increasingly dominant at higher values of the mass hypothesis.

Table 3: The upper limit at 95% CL on the $\sigma_{\mathrm{H}^{\pm}}\mathcal{B}(\mathrm{H}^{\pm}\to\mathrm{tb})$ with the single-lepton and dilepton final states combined.

$m_{\mathrm{H}^{\pm}}$ (GeV)	Expected limits (pb)					Observed limits (pb)
	-2 s.d.	-1 s.d.	median expected	+1 s.d.	+2 s.d.	
200	2.1	2.8	4.0	5.6	7.8	9.6
220	1.3	1.7	2.4	3.5	4.8	2.9
250	0.9	1.2	1.6	2.3	3.1	3.4
300	0.7	0.9	1.3	1.9	2.6	1.1
350	0.47	0.63	0.89	1.25	1.71	0.61
400	0.37	0.50	0.70	0.98	1.33	0.61
500	0.20	0.27	0.38	0.53	0.73	0.28
650	0.12	0.17	0.23	0.33	0.45	0.12
800	0.07	0.10	0.14	0.20	0.28	0.14
1000	0.051	0.069	0.097	0.137	0.187	0.091
1500	0.024	0.033	0.046	0.066	0.090	0.037
2000	0.015	0.020	0.028	0.040	0.056	0.020
2500	0.009	0.013	0.018	0.026	0.037	0.013
3000	0.007	0.009	0.013	0.019	0.027	0.011

The model-dependent upper limits are obtained by comparing the observed limit with the theoretical predictions. The MSSM $m_{\mathrm{h}}^{\mathrm{mod}-}$ benchmark scenario is designed to give a mass of

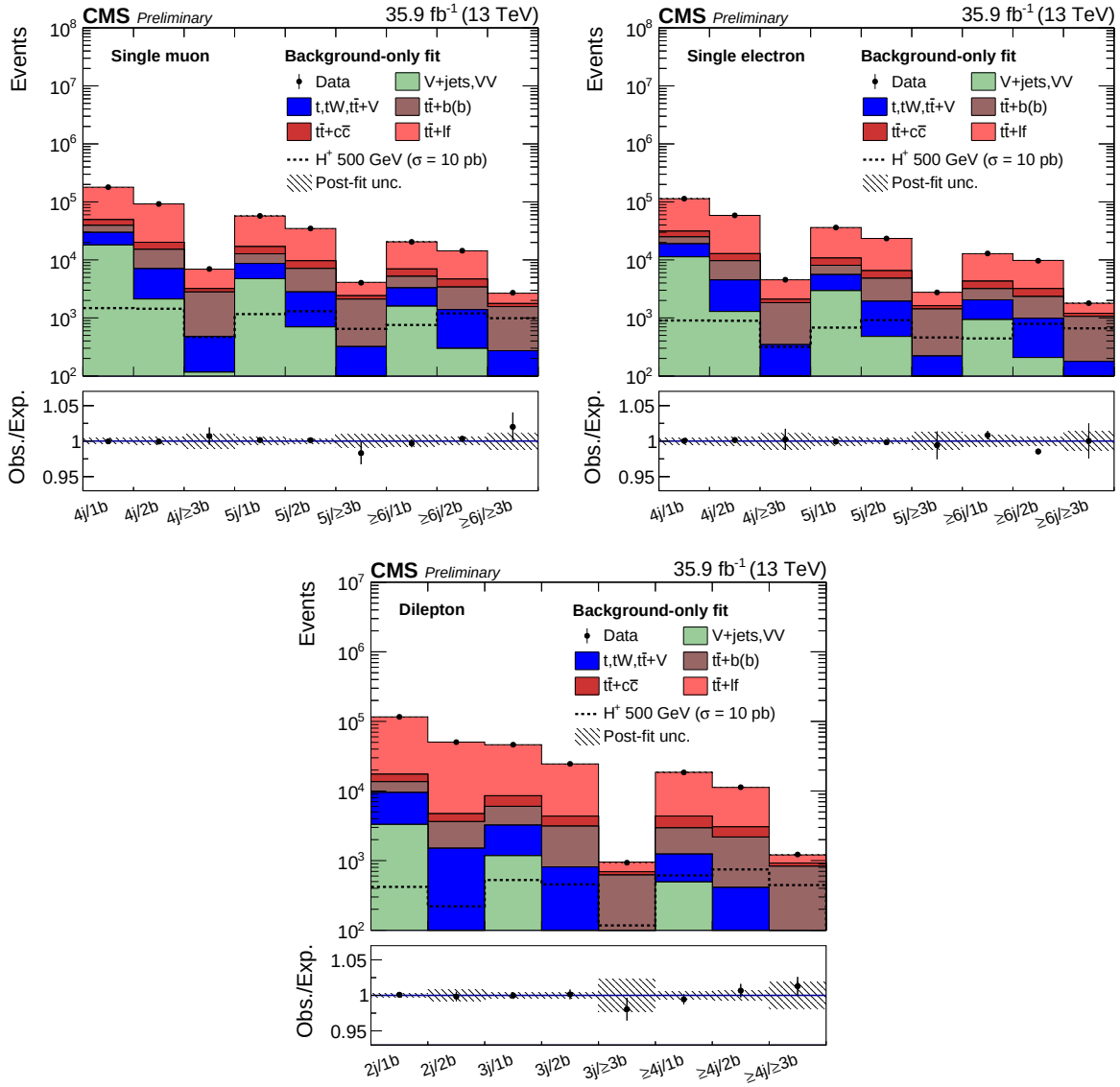

Figure 2: Summary of event yields in each analysis category for single-muon (top left), single-electron (top right), and dilepton (bottom) final states. The yields observed in data (black markers) are overlayed. The solid histograms represent the SM background prediction for $t\bar{t}$+LF (light red), $t\bar{t}$+c($\bar{c}$) (dark red), $t\bar{t}$+b($\bar{b}$) (brown), single top quark and $t\bar{t}$ in association with extra bosons (blue), and V+jets and multiboson production (light green). The dashed line represents the yields for a charged Higgs boson with a mass of 500 GeV and a product of the cross section and the branching fraction of 10 pb. The lower panel shows the ratio of data to the SM expectation after the background-only fit to the data and the hatched uncertainty bands include the total uncertainty.

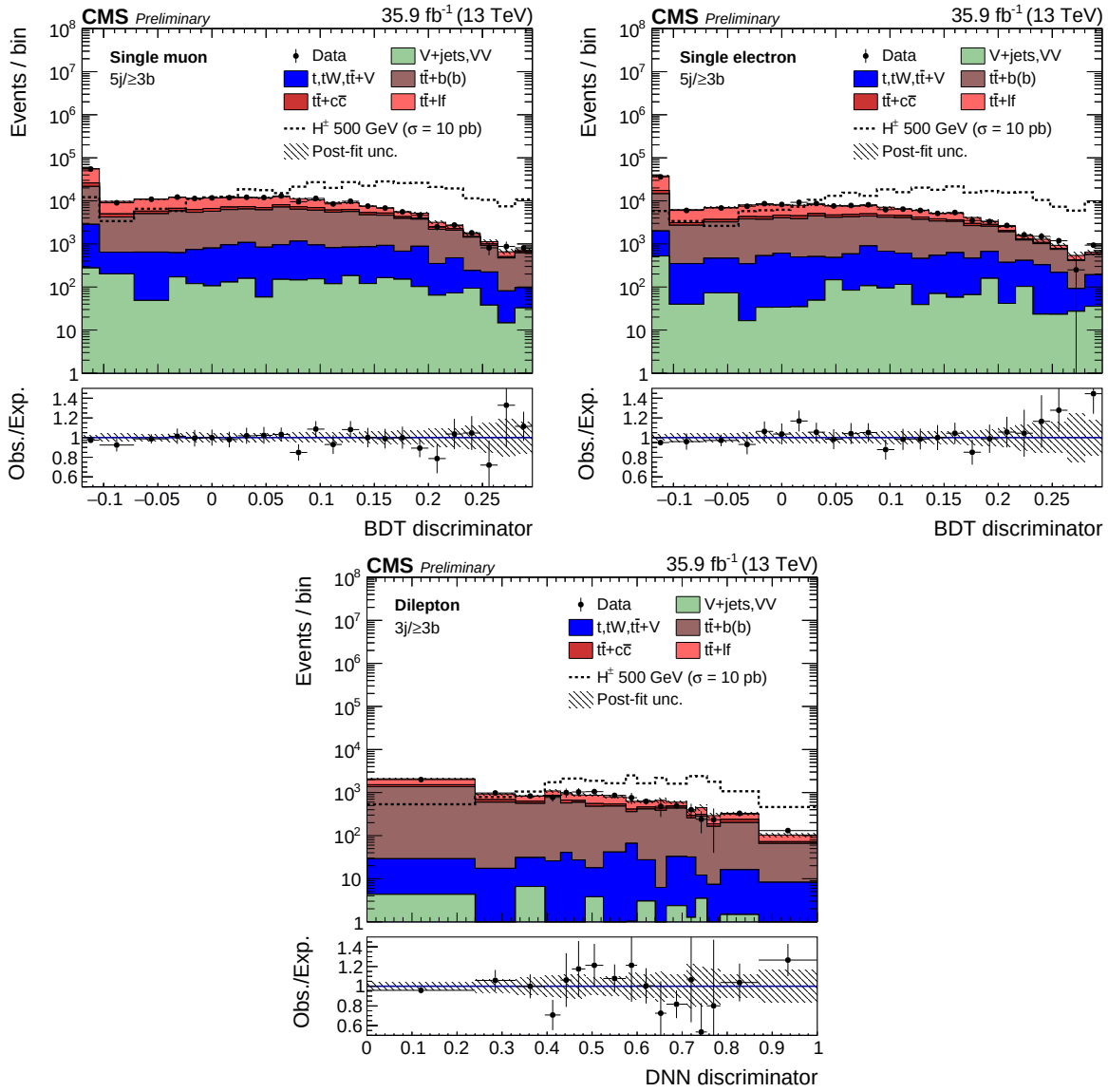

Figure 3: Distributions of the MVA outputs of the data and the SM expectation after the background-only fit to the data for the single-muon 5j/≥3b category(top left), for the single-electron 5j/≥3b category(top right), and for the dilepton 3j/≥3b category (bottom). The black markers show the data observation. The solid histograms represent the SM background prediction for $t\bar{t}$+LF (light red), $t\bar{t}$+c($\bar{c}$) (dark red), $t\bar{t}$+b($\bar{b}$) (brown), single top quark and $t\bar{t}$ in association with extra bosons (blue), and V+jets and multiboson production (light green). The dashed line represents the yields for a charged Higgs boson with a mass of 500 GeV and a product of the cross section and the branching fraction of 10 pb. The lower panel shows the ratio of data to the SM expectation after the background-only fit to the data and the hatched uncertainty bands include the total uncertainty.

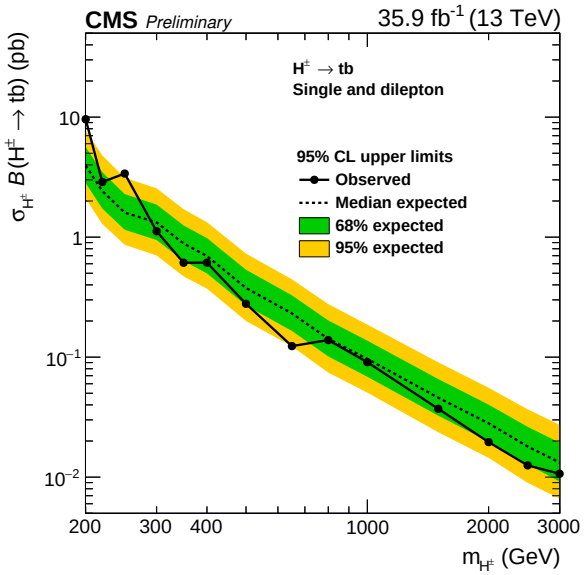

Figure 4: The upper limit at 95% CL on $\sigma_{\mathrm{H}^{\pm}}\mathcal{B}(\mathrm{H}^{\pm} \to \mathrm{tb})$ with single-lepton and dilepton final states combined. The solid black markers describe the observed upper limits, while the dashed line corresponds to the expectations from the SM background. The green (yellow) band represents one (two) standard deviation from the expected median.

approximately 125 GeV for the light CP-even Higgs boson over a wide region of the parameter space, while the $m_{\mathrm{h}}^{125}(\tilde{\chi})$ scenario is characterized by giving heavy mass to all supersymmetric particles with a phenomenology that resembles the Type-II 2HDM with MSSM-inspired Higgs couplings compatible with $m_{\mathrm{h}} \approx 125$ GeV for large masses of the m_{A} boson [10, 88, 89]. Figure 5 shows the excluded parameter space in the MSSM $m_{\mathrm{h}}^{\mathrm{mod}-}$ and $m_{\mathrm{h}}^{125}(\tilde{\chi})$ scenarios. In both models, the observed exclusion of high values of $\tan\beta$ is in the range 40–60 for $m_{\mathrm{H}^{\pm}}$ range 200–700 GeV; for low values of $\tan\beta$ the values 0.4–1.5 are excluded for $m_{\mathrm{H}^{\pm}}$ range 200 GeV–1.5 TeV in the context of $m_{\mathrm{h}}^{\mathrm{mod}-}$ while the values 0.6–1.5 are excluded for $m_{\mathrm{H}^{\pm}}$ range 200 GeV–1 TeV for the $m_{\mathrm{h}}^{125}(\tilde{\chi})$.

8 Summary

A search is presented for a charged Higgs boson decaying into a top-bottom quark-antiquark pair. The analyzed proton-proton collision data are collected with the CMS detector at the LHC and correspond to an integrated luminosity of 35.9 fb^{-1}. The search uses events with a single isolated charged lepton (electron or muon) or an opposite sign dilepton pair (electron or muon). Events are categorized according to the jet multiplicity and the number of jets identified as containing a b-hadron decay. Multivariate techniques are used to discriminate between signal and background events, the latter being dominated by $\mathrm{t\bar{t}}$ production. Results are presented for a charged Higgs boson with a mass larger than the top quark mass. 95% confidence level upper limits of 9.6–0.01 pb are set on the product of the charged Higgs production cross section and the branching fraction into top-bottom quark-antiquark pair in the mass range from 200 GeV to 3 TeV. Exclusion regions in the parameter space of the minimal supersymmetric standard model $m_{\mathrm{h}}^{\mathrm{mod}-}$ and $m_{\mathrm{h}}^{125}(\tilde{\chi})$ benchmark scenarios are presented.

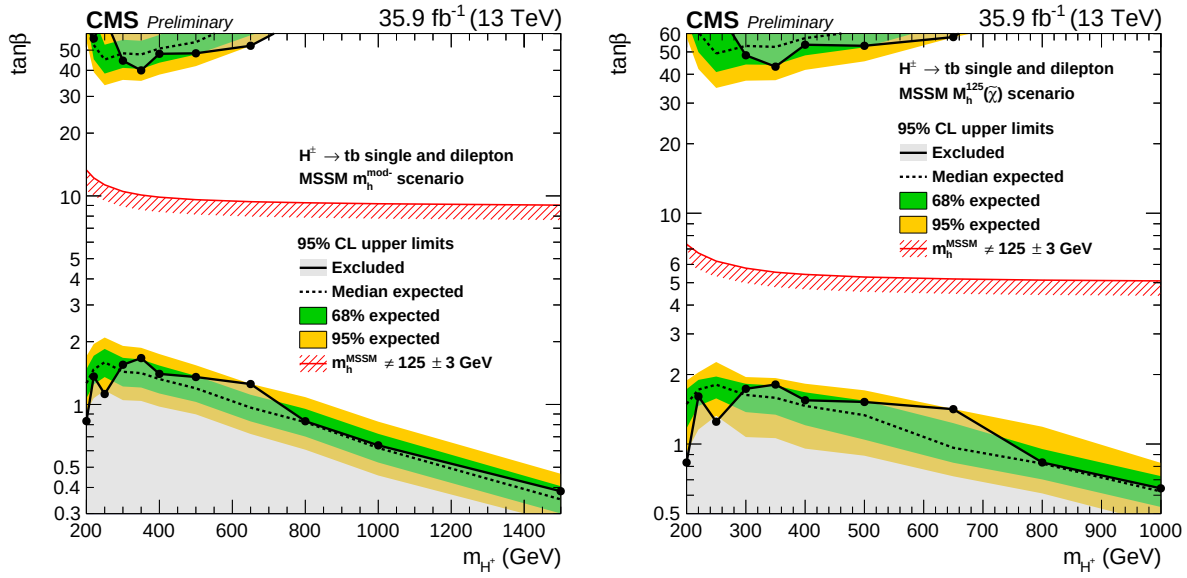

Figure 5: Excluded parameter space region in the $m_{\mathrm{h}}^{\mathrm{mod}-}$scenario (left) and in the $m_{\mathrm{h}}^{125}(\tilde{\chi})$ scenario (right). The grey area delimited by solid black line and markers represents the observed excluded region. The dashed black line and the green (yellow) regions represent the median expected exclusion regions and one (two) standard deviation from the expected median, respectively. The region below the red line is excluded assuming that the observed neutral Higgs boson is the light CP-even 2HDM Higgs boson with a mass of $125 \pm 3\,\mathrm{GeV}$, where the uncertainty is the theoretical uncertainty in the mass calculation.

References

[1] ATLAS Collaboration, "Observation of a new particle in the search for the standard model Higgs boson with the ATLAS detector at the LHC", *Phys. Lett. B* **716** (2012) 1, doi:10.1016/j.physletb.2012.08.020, arXiv:1207.7214.

[2] CMS Collaboration, "Observation of a new boson at a mass of 125 GeV with the CMS experiment at the LHC", *Phys. Lett. B* **716** (2012) 30, doi:10.1016/j.physletb.2012.08.021, arXiv:1207.7235.

[3] CMS Collaboration, "A new boson with a mass of 125 GeV observed with the CMS experiment at the Large Hadron Collider", *Science* **338** (2012) 1569, doi:10.1126/science.1230816.

[4] ATLAS and CMS Collaborations, "Combined measurement of the Higgs boson mass in pp collisions at $\sqrt{s} = 7$ and 8 TeV with the ATLAS and CMS experiments", *Phys. Rev. Lett.* **114** (2015) 191803, doi:10.1103/PhysRevLett.114.191803, arXiv:1503.07589.

[5] CMS Collaboration, "Measurements of properties of the Higgs boson decaying into the four-lepton final state in pp collisions at $\sqrt{s} = 13$ TeV", *JHEP* **11** (2017) 047, doi:10.1007/JHEP11(2017)047, arXiv:1706.09936.

[6] J. F. Gunion and H. E. Haber, "The CP conserving two Higgs doublet model: The approach to the decoupling limit", *Phys. Rev. D* **67** (2003) 075019, doi:10.1103/PhysRevD.67.075019, arXiv:hep-ph/0207010.

[7] A. G. Akeroyd et al., "Prospects for charged Higgs searches at the LHC", *Eur. Phys. J. C* **77** (2017) 276, doi:10.1140/epjc/s10052-017-4829-2, arXiv:1607.01320.

[8] G. C. Branco et al., "Theory and phenomenology of two-Higgs-doublet models", *Phys. Rept.* **516** (2012) 1, doi:10.1016/j.physrep.2012.02.002, arXiv:1106.0034.

[9] A. Djouadi, "The anatomy of electro-weak symmetry breaking. II. The Higgs bosons in the minimal supersymmetric model", *Phys. Rept.* **459** (2008) 1, doi:10.1016/j.physrep.2007.10.005, arXiv:hep-ph/0503173.

[10] M. Carena et al., "MSSM Higgs boson searches at the LHC: benchmark scenarios after the discovery of a Higgs-like particle", *Eur. Phys. J. C* **73** (2013) 2552, doi:10.1140/epjc/s10052-013-2552-1, arXiv:1302.7033.

[11] R. Harlander, M. Kramer, and M. Schumacher, "Bottom-quark associated Higgs-boson production: reconciling the four- and five-flavour scheme approach", Technical Report CERN-PH-TH-2011-134, 2011. arXiv:1112.3478.

[12] LHC Higgs Cross Section Working Group Collaboration, "Handbook of LHC Higgs cross sections: 4. deciphering the nature of the Higgs sector", doi:10.23731/CYRM-2017-002, arXiv:1610.07922.

[13] ALEPH, DELPHI, L3, OPAL, LEP Collaboration, "Search for charged Higgs bosons: combined results using LEP Data", *Eur. Phys. J. C* **73** (2013) 2463, doi:10.1140/epjc/s10052-013-2463-1, arXiv:1301.6065.

[14] CDF Collaboration, "Search for Higgs bosons predicted in two-Higgs-doublet models via decays to tau lepton pairs in 1.96-TeV p anti-p collisions", *Phys. Rev. Lett.* **103** (2009) 201801, doi:10.1103/PhysRevLett.103.201801, arXiv:0906.1014.

[15] D0 Collaboration, "Search for Higgs bosons of the minimal supersymmetric standard model in $p\bar{p}$ collisions at $\sqrt{(s)} = 1.96$ TeV", *Phys. Lett. B* **710** (2012) 569, doi:10.1016/j.physletb.2012.03.021, arXiv:1112.5431.

[16] A. Arbey, F. Mahmoudi, O. Stal, and T. Stefaniak, "Status of the charged Higgs boson in two Higgs doublet models", *Eur. Phys. J. C* **78** (2018) 182, doi:10.1140/epjc/s10052-018-5651-1, arXiv:1706.07414.

[17] CMS Collaboration, "Search for a charged Higgs boson in pp collisions at $\sqrt{s} = 8$ TeV", *JHEP* **11** (2015) 018, doi:10.1007/JHEP11(2015)018, arXiv:1508.07774.

[18] ATLAS Collaboration, "Search for charged Higgs bosons in the $H^{\pm} \to tb$ decay channel in pp collisions at $\sqrt{s} = 8$ TeV using the ATLAS detector", *JHEP* **03** (2016) 127, doi:10.1007/JHEP03(2016)127, arXiv:1512.03704.

[19] ATLAS Collaboration, "Search for charged Higgs bosons decaying into top and bottom quarks at $\sqrt{s} = 13$ TeV with the ATLAS detector", *JHEP* **11** (2018) 085, doi:10.1007/JHEP11(2018)085, arXiv:1808.03599.

[20] ATLAS Collaboration, "Search for charged Higgs bosons decaying via $H^{\pm} \to \tau^{\pm}\nu_{\tau}$ in the τ+jets and τ+lepton final states with 36 fb^{-1} of pp collision data recorded at $\sqrt{s} = 13$ TeV with the ATLAS experiment", *JHEP* **09** (2018) 139, doi:10.1007/JHEP09(2018)139, arXiv:1807.07915.

[21] ATLAS Collaboration, "Search for charged Higgs bosons produced in association with a top quark and decaying via $H^{\pm} \to \tau\nu$ using pp collision data recorded at $\sqrt{s} = 13$ TeV by the ATLAS detector", *Phys. Lett. B* **759** (2016) 555, doi:10.1016/j.physletb.2016.06.017, arXiv:1603.09203.

[22] ATLAS Collaboration, "Search for charged Higgs bosons decaying via $H^{\pm} \to \tau^{\pm}\nu$ in fully hadronic final states using pp collision data at $\sqrt{s} = 8$ TeV with the ATLAS detector", *JHEP* **03** (2015) 088, doi:10.1007/JHEP03(2015)088, arXiv:1412.6663.

[23] CMS Collaboration, "Search for a light charged Higgs boson decaying to $c\bar{s}$ in pp collisions at $\sqrt{s} = 8$ TeV", *JHEP* **12** (2015) 178, doi:10.1007/JHEP12(2015)178, arXiv:1510.04252.

[24] CMS Collaboration, "Search for a charged Higgs boson decaying to charm and bottom quarks in proton-proton collisions at $\sqrt{s} = 8$ TeV", *JHEP* **11** (2018) 115, doi:10.1007/JHEP11(2018)115, arXiv:1808.06575.

[25] CMS Collaboration, "Search for charged Higgs bosons produced via vector boson fusion and decaying into a pair of W and Z bosons using pp collisions at $\sqrt{s} = 13$ TeV", *Phys. Rev. Lett.* **119** (2017) 141802, doi:10.1103/PhysRevLett.119.141802, arXiv:1705.02942.

[26] CMS Collaboration, "Search for beyond the standard model Higgs bosons decaying into a $b\bar{b}$ pair in pp collisions at $\sqrt{s} = 13$ TeV", *JHEP* **08** (2018) 113, doi:10.1007/JHEP08(2018)113, arXiv:1805.12191.

[27] CMS Collaboration, "Search for additional neutral MSSM Higgs bosons in the $\tau\tau$ final state in proton-proton collisions at $\sqrt{s} = 13$ TeV", *JHEP* **09** (2018) 007, doi:10.1007/JHEP09(2018)007, arXiv:1803.06553.

[28] ATLAS Collaboration, "Search for additional heavy neutral Higgs and gauge bosons in the ditau final state produced in 36 fb^{-1} of pp collisions at $\sqrt{s}$ = 13 TeV with the ATLAS detector", *JHEP* **01** (2018) 055, doi:10.1007/JHEP01(2018)055, arXiv:1709.07242.

[29] ATLAS Collaboration, "Search for heavy Higgs bosons A/H decaying to a top quark pair in pp collisions at $\sqrt{s}$ = 8 TeV with the ATLAS detector", *Phys. Rev. Lett.* **119** (2017) 191803, doi:10.1103/PhysRevLett.119.191803, arXiv:1707.06025.

[30] CMS Collaboration, "Search for physics beyond the standard model in events with two leptons of same sign, missing transverse momentum, and jets in proton-proton collisions at $\sqrt{s}$ = 13 TeV", *Eur. Phys. J. C* **77** (2017) 578, doi:10.1140/epjc/s10052-017-5079-z, arXiv:1704.07323.

[31] CMS Collaboration, "The CMS trigger system", *JINST* **12** (2017) P01020, doi:10.1088/1748-0221/12/01/P01020, arXiv:1609.02366.

[32] CMS Collaboration, "The CMS experiment at the CERN LHC", *JINST* **3** (2008) S08004, doi:10.1088/1748-0221/3/08/S08004.

[33] J. Alwall et al., "The automated computation of tree-level and next-to-leading order differential cross sections, and their matching to parton shower simulations", *JHEP* **07** (2014) 079, doi:10.1007/JHEP07(2014)079, arXiv:1405.0301.

[34] S. Frixione, P. Nason, and C. Oleari, "Matching NLO QCD computations with parton shower simulations: the POWHEG method", *JHEP* **11** (2007) 070, doi:10.1088/1126-6708/2007/11/070, arXiv:0709.2092.

[35] J. Alwall et al., "Comparative study of various algorithms for the merging of parton showers and matrix elements in hadronic collisions", *Eur. Phys. J. C* **53** (2008) 473, doi:10.1140/epjc/s10052-007-0490-5, arXiv:0706.2569.

[36] R. Frederix and S. Frixione, "Merging meets matching in MC@NLO", *JHEP* **12** (2012) 061, doi:10.1007/JHEP12(2012)061, arXiv:1209.6215.

[37] NNPDF Collaboration, "Parton distributions for the LHC Run II", *JHEP* **04** (2015) 040, doi:10.1007/JHEP04(2015)040, arXiv:1410.8849.

[38] T. Sjöstrand et al., "An introduction to PYTHIA 8.2", *Comput. Phys. Commun.* **191** (2015) 159, doi:10.1016/j.cpc.2015.01.024, arXiv:1410.3012.

[39] P. Skands, S. Carrazza, and J. Rojo, "Tuning PYTHIA 8.1: the Monash 2013 tune", *Eur. Phys. J. C* **74** (2014) 3024, doi:10.1140/epjc/s10052-014-3024-y, arXiv:1404.5630.

[40] CMS Collaboration, "Event generator tunes obtained from underlying event and multiparton scattering measurements", *Eur. Phys. J. C* **76** (2016) 155, doi:10.1140/epjc/s10052-016-3988-x, arXiv:1512.00815.

[41] S. Heinemeyer, W. Hollik, and G. Weiglein, "FeynHiggs: a program for the calculation of the masses of the neutral CP even Higgs bosons in the MSSM", *Comput. Phys. Commun.* **124** (2000) 76, doi:10.1016/S0010-4655(99)00364-1, arXiv:hep-ph/9812320.

[42] E. L. Berger, T. Han, J. Jiang, and T. Plehn, "Associated production of a top quark and a charged Higgs boson", *Phys. Rev. D* **71** (2005) 115012, doi:10.1103/PhysRevD.71.115012, arXiv:hep-ph/0312286.

[43] M. Flechl et al., "Improved cross-section predictions for heavy charged Higgs boson production at the LHC", *Phys. Rev. D* **91** (2015) 075015, doi:10.1103/PhysRevD.91.075015, arXiv:1409.5615.

[44] C. Degrande, M. Ubiali, M. Wiesemann, and M. Zaro, "Heavy charged Higgs boson production at the LHC", *JHEP* **10** (2015) 145, doi:10.1007/JHEP10(2015)145, arXiv:1507.02549.

[45] S. Dittmaier, M. Kramer, M. Spira, and M. Walser, "Charged-Higgs-boson production at the LHC: NLO supersymmetric QCD corrections", *Phys. Rev. D* **83** (2011) 055005, doi:10.1103/PhysRevD.83.055005, arXiv:0906.2648.

[46] A. Djouadi, J. Kalinowski, and M. Spira, "HDECAY: a program for Higgs boson decays in the standard model and its supersymmetric extension", *Comput. Phys. Commun.* **108** (1998) 56, doi:10.1016/S0010-4655(97)00123-9, arXiv:hep-ph/9704448.

[47] M. Cacciari et al., "Top-pair production at hadron colliders with next-to-next-to-leading logarithmic soft-gluon resummation", *Phys. Lett. B* **710** (2012) 612, doi:10.1016/j.physletb.2012.03.013, arXiv:1111.5869.

[48] P. Barnreuther, M. Czakon, and A. Mitov, "Percent level precision physics at the Tevatron: first genuine NNLO QCD corrections to $q\bar{q} \to t\bar{t} + X$", *Phys. Rev. Lett.* **109** (2012) 132001, doi:10.1103/PhysRevLett.109.132001, arXiv:1204.5201.

[49] M. Czakon and A. Mitov, "NNLO corrections to top-pair production at hadron colliders: the all-fermionic scattering channels", *JHEP* **12** (2012) 054, doi:10.1007/JHEP12(2012)054, arXiv:1207.0236.

[50] M. Czakon and A. Mitov, "NNLO corrections to top pair production at hadron colliders: the quark-gluon reaction", *JHEP* **01** (2013) 080, doi:10.1007/JHEP01(2013)080, arXiv:1210.6832.

[51] M. Beneke, P. Falgari, S. Klein, and C. Schwinn, "Hadronic top-quark pair production with NNLL threshold resummation", *Nucl. Phys. B* **855** (2012) 695, doi:10.1016/j.nuclphysb.2011.10.021, arXiv:1109.1536.

[52] M. Czakon, P. Fiedler, and A. Mitov, "Total top-quark pair-production cross section at hadron colliders through $O(\frac{4}{5})$", *Phys. Rev. Lett.* **110** (2013) 252004, doi:10.1103/PhysRevLett.110.252004, arXiv:1303.6254.

[53] M. Czakon and A. Mitov, "Top++: a program for the calculation of the top-pair cross-section at hadron colliders", *Comput. Phys. Commun.* **185** (2014) 2930, doi:10.1016/j.cpc.2014.06.021, arXiv:1112.5675.

[54] M. Aliev et al., "HATHOR: hadronic top and heavy quarks cross section calculator", *Comput. Phys. Commun.* **182** (2011) 1034, doi:10.1016/j.cpc.2010.12.040, arXiv:1007.1327.

[55] P. Kant et al., "HATHOR for single top-quark production: updated predictions and uncertainty estimates for single top-quark production in hadronic collisions", *Comput. Phys. Commun.* **191** (2015) 74, doi:10.1016/j.cpc.2015.02.001, arXiv:1406.4403.

[56] F. Maltoni, D. Pagani, and I. Tsinikos, "Associated production of a top-quark pair with vector bosons at NLO in QCD: impact on $t\bar{t}H$ searches at the LHC", *JHEP* **02** (2016) 113, doi:10.1007/JHEP02(2016)113, arXiv:1507.05640.

[57] J. M. Campbell, R. K. Ellis, and C. Williams, "Vector boson pair production at the LHC", *JHEP* **07** (2011) 018, doi:10.1007/JHEP07(2011)018, arXiv:1105.0020.

[58] N. Kidonakis, "Two-loop soft anomalous dimensions for single top quark associated production with a W^- or H^-", *Phys. Rev. D* **82** (2010) 054018, doi:10.1103/PhysRevD.82.054018, arXiv:1005.4451.

[59] GEANT4 Collaboration, "GEANT4—a simulation toolkit", *Nucl. Instrum. Meth. A* **506** (2003) 250, doi:10.1016/S0168-9002(03)01368-8.

[60] CMS Collaboration, "Particle-flow reconstruction and global event description with the CMS detector", *JINST* **12** (2017) P10003, doi:10.1088/1748-0221/12/10/P10003, arXiv:1706.04965.

[61] CMS Collaboration, "Description and performance of track and primary-vertex reconstruction with the CMS tracker", *JINST* **9** (2014) P10009, doi:10.1088/1748-0221/9/10/P10009, arXiv:1405.6569.

[62] M. Cacciari, G. P. Salam, and G. Soyez, "The anti-k_T jet clustering algorithm", *JHEP* **04** (2008) 063, doi:10.1088/1126-6708/2008/04/063, arXiv:0802.1189.

[63] M. Cacciari, G. P. Salam, and G. Soyez, "FastJet user manual", *Eur. Phys. J. C* **72** (2012) 1896, doi:10.1140/epjc/s10052-012-1896-2, arXiv:1111.6097.

[64] CMS Collaboration, "Performance of electron reconstruction and selection with the CMS detector in proton-proton collisions at $\sqrt{s} = 8$ TeV", *JINST* **10** (2015) P06005, doi:10.1088/1748-0221/10/06/P06005, arXiv:1502.02701.

[65] CMS Collaboration, "Performance of the CMS muon detector and muon reconstruction with proton-proton collisions at $\sqrt{s} = 13$ TeV", *JINST* **13** (2018) P06015, doi:10.1088/1748-0221/13/06/P06015, arXiv:1804.04528.

[66] CMS Collaboration, "Jet algorithms performance in 13 TeV data", CMS Physics Analysis Summary CMS-PAS-JME-16-003, CERN, 2017.

[67] CMS Collaboration, "Identification of b-quark jets with the CMS experiment", *JINST* **8** (2013) P04013, doi:10.1088/1748-0221/8/04/P04013, arXiv:1211.4462.

[68] CMS Collaboration, "Performance of the CMS missing transverse momentum reconstruction in pp data at $\sqrt{s}$ = 8 TeV", *JINST* **10** (2015) P02006, doi:10.1088/1748-0221/10/02/P02006, arXiv:1411.0511.

[69] CMS Collaboration, "Performance of reconstruction and identification of τ leptons decaying to hadrons and ν_τ in pp collisions at $\sqrt{s} = 13$ TeV", *JINST* **13** (2018), no. 10, P10005, doi:10.1088/1748-0221/13/10/P10005, arXiv:1809.02816.

[70] G. C. Fox and S. Wolfram, "Observables for the analysis of event shapes in e^+e^- annihilation and other processes", *Phys. Rev. Lett.* **41** (1978) 1581, doi:10.1103/PhysRevLett.41.1581.

[71] J. F. T. Hastie, R. Tibshirani, "The elements of statistical learning". Springer-Verlag, 2009, 10th printing 2013.

[72] A. Hoecker et al., "TMVA – toolkit for multivariate data analysis", in *Proceedings, 11th international workshop on advanced computing and analysis techniques in physics research (ACAT 2007): Amsterdam, Netherlands, April 23–27, 2007*, volume ACAT, p. 040. 2007. arXiv:physics/0703039.

[73] P. Baldi et al., "Parameterized neural networks for high-energy physics", *Eur. Phys. J. C* **76** (2016) 235, doi:10.1140/epjc/s10052-016-4099-4, arXiv:1601.07913.

[74] M. Abadi et al., "TensorFlow: large-scale machine learning on heterogeneous systems", 2015. https://www.tensorflow.org.

[75] F. Chollet et al., "Keras", 2015. https://keras.io.

[76] ATLAS and CMS Collaborations, "Procedure for the LHC Higgs boson search combination in Summer 2011", Technical Report CMS-NOTE-2011-005. ATL-PHYS-PUB-2011-11, CERN, 2011.

[77] CMS Collaboration, "CMS luminosity measurements for the 2016 data taking period", CMS Physics Analysis Summary CMS-PAS-LUM-17-001, 2017.

[78] ATLAS Collaboration, "Measurement of the inelastic proton-proton cross section at $\sqrt{s} = 13$ TeV with the ATLAS detector at the LHC", *Phys. Rev. Lett.* **117** (2016) 182002, doi:10.1103/PhysRevLett.117.182002, arXiv:1606.02625.

[79] CMS Collaboration, "Identification of heavy-flavour jets with the CMS detector in pp collisions at 13 TeV", *JINST* **13** (2018) P05011, doi:10.1088/1748-0221/13/05/P05011, arXiv:1712.07158.

[80] J. Butterworth et al., "PDF4LHC recommendations for LHC Run II", *J. Phys. G* **43** (2016) 023001, doi:10.1088/0954-3899/43/2/023001, arXiv:1510.03865.

[81] CMS Collaboration, "Investigations of the impact of the parton shower tuning in PYTHIA 8 in the modelling of $\mathrm{t\bar{t}}$ at $\sqrt{s} = 8$ and 13 TeV", CMS Physics Analysis Summary CMS-PAS-TOP-16-021, 2016.

[82] T. Jeo, J. M. Lindert, N. Moretti, and S. Pozzorini, "New NLOPS predictions for $t\bar{t} + b$ -jet production at the LHC", *Eur. Phys. J. C* **78** (2018) 502, doi:10.1140/epjc/s10052-018-5956-0, arXiv:1802.00426.

[83] R. Barlow and C. Beeston, "Fitting using finite Monte Carlo samples", *Comput. Phys. Commun.* **77** (1993) 219, doi:10.1016/0010-4655(93)90005-W.

[84] J. S. Conway, "Incorporating nuisance parameters in likelihoods for multisource spectra", in *Proceedings, PHYSTAT 2011 workshop on statistical issues related to discovery claims in search experiments and unfolding, CERN, Geneva, Switzerland 17–20 January 2011*, p. 115. 2011. arXiv:1103.0354. doi:10.5170/CERN-2011-006.115.

[85] G. Cowan, K. Cranmer, E. Gross, and O. Vitells, "Asymptotic formulae for likelihood-based tests of new physics", *Eur. Phys. J. C* **71** (2011) 1554, doi:10.1140/epjc/s10052-011-1554-0, arXiv:1007.1727. [Erratum: doi:10.1140/epjc/s10052-013-2501-z].

[86] A. L. Read, "Presentation of search results: The CL_s technique", *J. Phys. G* **28** (2002) 2693, doi:10.1088/0954-3899/28/10/313.

[87] T. Junk, "Confidence level computation for combining searches with small statistics", *Nucl. Instrum. Meth. A* **434** (1999) 435, doi:10.1016/S0168-9002(99)00498-2, arXiv:hep-ex/9902006.

[88] E. Bagnaschi et al., "Benchmark scenarios for low tan β in the MSSM", Technical Report LHCHXSWG-2015-002, CERN, Geneva, 2015.

[89] H. Bahl et al., "MSSM Higgs boson searches at the LHC: benchmark scenarios for run 2 and beyond", arXiv:1808.07542.